

Laboratory and Sky Testing Results for the TIS H4RG-10 4k x 4k, 10 micron visible CMOS-Hybrid Detector

Bryan N. Dorland^{*a}, Gregory S. Hennessy^a, Norbert Zacharias^a, David G. Monet^b, Hugh Harris^b, Chris Rollins^c, Peter Shu^d, Laddawan Miko^d, Brent Mott^d, Augustyn Waczynski^e, Emily Kan^e, Gregory Delo^e

^aUnited States Naval Observatory, 3450 Massachusetts Avenue NW, Washington, DC 20392;

^bUnited States Naval Observatory, Flagstaff Station, 10391 West Naval Observatory Road, Flagstaff, AZ 86001;

^cResearch Support Instruments, 4325-B Forbes Blvd., Lanham, MD 20706;

^dDetector Systems Branch, NASA/Goddard Space Flight Center, 8800 Greenbelt Road, Greenbelt, MD 20771;

^eGlobal Science and Technology, Inc., 7855 Walker Drive, Suite 200, Greenbelt, MD 20770

ABSTRACT

We present both laboratory and telescope testing results describing the performance of the H4RG-10 CMOS-Hybrid detector. The H4RG-10 is the largest visible hybrid array currently in existence and shows great potential for use in future space missions. We report read noise, dark current, pixel connectivity, persistence, and inter-pixel capacitance measurements for the temperature range 110–240 K. We report on quantitative astrometric and qualitative photometric performance of the instrument based on observations made at USNO's Flagstaff Station observatory and establish an upper limit to the astrometric performance of the detector. We discuss additional testing and future work associated with improving detector performance.

Keywords: CMOS-Hybrid, performance testing, astrometric testing

1. INTRODUCTION

For many years, Charge Coupled Detectors (CCDs) have been the only acceptable detector solution for high-performance, space-based visible instrumentation. This is especially true for astronomical applications, which typically require very low noise and very low dark currents in order to observe very faint targets and perform measurements on these targets at very high precision. CCDs have, historically, been the only detectors capable of supplying the required very low noise and dark current levels.

Complimentary Metal Oxide Semiconductor (CMOS) technology provides many capabilities that CCDs do not. The CMOS readout integrated circuitry (ROIC), for example, is extremely flexible, and can, in principle, provide fully electronic shuttering, including both rolling⁺ and “snapshot”[&] readout modes; non-destructive reads wherein data are read out from the focal plane without interrupting integration; random access windowing that allows specific pixels to be read out rather than the entire array; and random access pixel reset that allows resetting a selected subset of the pixels to avoid, e.g., saturation due to the presence of a bright star. Furthermore, since CMOS pixels are read out directly, the problematic effects of displacement damage in the silicon are greatly reduced vs. CCDs, making CMOS detectors much less sensitive to the high-energy proton damage that occurs in space (see, e.g., [1] and references therein). CMOS detectors also typically use much less power (and, as a result, produce

* email: bdorland@usno.navy.mil

⁺ i.e., starting and stopping the integration of each pixel sequentially

[&] i.e., starting and stopping the integration of all pixels at the same time

Report Documentation Page

Form Approved
OMB No. 0704-0188

Public reporting burden for the collection of information is estimated to average 1 hour per response, including the time for reviewing instructions, searching existing data sources, gathering and maintaining the data needed, and completing and reviewing the collection of information. Send comments regarding this burden estimate or any other aspect of this collection of information, including suggestions for reducing this burden, to Washington Headquarters Services, Directorate for Information Operations and Reports, 1215 Jefferson Davis Highway, Suite 1204, Arlington VA 22202-4302. Respondents should be aware that notwithstanding any other provision of law, no person shall be subject to a penalty for failing to comply with a collection of information if it does not display a currently valid OMB control number.

1. REPORT DATE 2007	2. REPORT TYPE	3. DATES COVERED 00-00-2007 to 00-00-2007	
4. TITLE AND SUBTITLE Laboratory And Sky Testing Results For The TIS H4RG-10 4k -4k 10-micron Visible CMOS-Hybrid Detector		5a. CONTRACT NUMBER	
		5b. GRANT NUMBER	
		5c. PROGRAM ELEMENT NUMBER	
6. AUTHOR(S)		5d. PROJECT NUMBER	
		5e. TASK NUMBER	
		5f. WORK UNIT NUMBER	
7. PERFORMING ORGANIZATION NAME(S) AND ADDRESS(ES) U.S. Naval Observatory, 3450 Massachusetts Avenue, N.W., Washington, DC, 20392		8. PERFORMING ORGANIZATION REPORT NUMBER	
9. SPONSORING/MONITORING AGENCY NAME(S) AND ADDRESS(ES)		10. SPONSOR/MONITOR'S ACRONYM(S)	
		11. SPONSOR/MONITOR'S REPORT NUMBER(S)	
12. DISTRIBUTION/AVAILABILITY STATEMENT Approved for public release; distribution unlimited			
13. SUPPLEMENTARY NOTES Proc. of SPIE Vol. 6690, 66900D, (2007)			
14. ABSTRACT We present both laboratory and telescope testing results describing the performance of the H4RG-10 CMOS-Hybrid detector. The H4RG-10 is the largest visible hybrid array currently in existence and shows great potential for use in future space missions. We report read noise, dark current, pixel connectivity, persistence, and inter-pixel capacitance measurements for the temperature range 110-240 K. We report on quantitative astrometric and qualitative photometric performance of the instrument based on observations made at USNO's Flagstaff Station observatory and establish an upper limit to the astrometric performance of the detector. We discuss additional testing and future work associated with improving detector performance.			
15. SUBJECT TERMS			
16. SECURITY CLASSIFICATION OF:			17. LIMITATION OF ABSTRACT
a. REPORT unclassified	b. ABSTRACT unclassified	c. THIS PAGE unclassified	
			18. NUMBER OF PAGES 15
			19a. NAME OF RESPONSIBLE PERSON

much less heat) than CCDs, and there exists a growing industrial base for building large quantities of inexpensive and increasingly capable CMOS detectors for consumer electronics applications such as cell phone cameras.

Unfortunately, monolithic* CMOS detectors have had many drawbacks for high-performance applications. The implantation of the readout circuitry on the photosensitive surface reduces the effective photosensitive area of the detector, and as the pixel size shrinks, the relative “optically dead area” increases until the readout circuit occupies the entire pixel. For detectors not at this limit, the ROIC structure results in intra-pixel response variations that can be dependent on the focal ratio of the incoming beam. The proximity of the implanted circuitry in one pixel to that in neighboring pixels—especially with smaller pixels—can result in inter-pixel capacitance that is manifested as inter-pixel cross-talk. Finally, the read noise performance for CMOS has historically been unable to match that of CCDs. For these reasons, astronomical applications have, for the most part, eschewed the use of CMOS detectors (see [2] and [3] for recent test results from a 5 micron monolithic CMOS detector), preferring CCDs instead.

As Janesick has discussed [4], new technologies are now being developed that attempt to match the excellent performance of CCDs with the flexibility of the CMOS ROIC. The first of these new approaches, and the one we are concerned with in this paper, is the “CMOS-Hybrid”⁺, which mates a silicon detector with a CMOS ROIC. Use of a dedicated detector layer with all circuitry located on the back results in 100% fill factor on the front. Separation of the ROIC circuitry from the detector allows for optimization of circuit placement without regard to impact on the photosensitive region. Other technologies such as backside-CMOS [e.g., 5, 6] are also under development which seek to address this problem using alternate techniques. Our assessment is that these alternatives, while having great promise for the future, are longer-term solutions than the hybridization approach used for CMOS-Hybrids which have been proven at some level for both visible and infra-red (IR) applications. For near-term applications, therefore, development and testing of the latter are extremely important.

In this paper we discuss Teledyne Imaging Sensor’s (TIS)[#] H4RG-10 CMOS-Hybrid Focal Plane Assembly (FPA)[@]. The H4RG-10 is a large format (16.7 Mpix) CMOS-Hybrid FPA designed specifically for astronomical use. USNO procured a science grade unit (SGU) from the first lot run of the H4RG-10, and, in collaboration with Goddard Space Flight Center’s (GSFC) Detector Systems Branch (DSB) Detector Characterization Laboratory (DCL), fabricated a camera, and performed optimization, laboratory performance testing and sky testing at USNO’s dark sky site, Naval Observatory, Flagstaff Station (NOFS). In this paper, we report on these results, discuss implications for astrometric and photometric users of this detector and describe future plans. It is our intent to ultimately fly some form of CMOS-based detector in space as an astrometric and photometric sensor. The development and testing described in this paper are part of that effort.

2. H4RG-10 CMOS-HYBRID FPA

The H4RG-10 consists of a 4096 x 4096 array of pixels, each 10 microns square. The detector layer is a 100-micron thick Si P-i-N diode structure connected to the ROIC by means of a single indium bump-bond per pixel. The FPA provides a total of 64 output ports.

USNO requirements for the FPA are given in Table 1. Most of the parameters are self-explanatory. Full Well Capacity (FWC) was defined in terms of non-linearity of the response. Pixel operability was defined in terms of number of pixels providing at least 50% throughput for a given input signal. In addition to the performance parameters, we required the FPA to support random access windowing (i.e., reading out one or more subsections of the array rather than the entire array), non-destructive read (i.e., the ability to read one or more pixels out without disturbing the integration), and random access reset (i.e., the ability to reset selected pixels independently of the entire array).

* i.e., a detector and ROIC combined on a single silicon integrated circuit.

⁺ Sometimes referred to as a “CCD-CMOS Hybrid.”

[#] Formerly Rockwell Scientific Corporation (RSC).

[@] Here, we are using the term “FPA” to denote a single, integrated sensor consisting of detector layer, ROIC and the connecting bump bonds.

Given the history of earlier TIS CMOS-Hybrid FPAs such as the H2RG [7], we were less concerned with the ability of the FPA to meet these performance parameter goals and were more concerned with hybridization yield and electronics cross-talk. It was our assessment that the ability to correctly deposit, align and connect nearly 17 million In bumps would prove to be extremely challenging, and could have a significant negative impact on overall FPA yield. Given the small size of the pixels, the presence of bonds and implants and the proximity of the pixel circuitry with its neighbors, we were also highly concerned about cross-talk due to inter-pixel capacitance (IPC). Experience with larger pixels (i.e., 28 and 18 microns) suggested that as pixel size decreases, cross-talk increases and is due primarily to IPC issues rather than diffusion [8]. Going to 10 microns, this would obviously be an even larger concern.

Table 1. USNO Requirements for H4RG-10 FPA. Rightmost column indicates actual measured results to date.

<i>Parameter</i>	<i>Threshold</i>	<i>Objective</i>	<i>Measured</i>
Post-CDS read noise	< 10 e- RMS		7 e- RMS
Dark current	< 1 e- per pixel per second @ 193 K (mode)		30—40 e- per pixel @ 193 K
Full well capacity (FWC)	> 70,000 e-	> 100,000 e-	TBR
Spectral range Full Width Half Maximum (FWHM) (nm)	525—775	400—1000	450—975
Quantum Efficiency * Fill Factor (QE*FF) in reference spectral band	> 70%	> 90%	> 80%
Pixel operability	> 96%	> 99%	99.8%

USNO understood that these detectors were to be from the first lot run of these devices. As such, the primary goal of the procurement was to obtain a functioning device suitable for characterization rather than a final, flight-grade unit. Given that this was a “best effort” activity, the parameters listed in Table 1 represent goals rather than hard and fast acceptance criteria.

USNO took delivery of a bare multiplexer (MUX) in mid-2006 and the science grade unit in February 2007 (see fig. 1). We are also in receipt of a loaned engineering grade unit (EGU) that was used initially for electronics set up and testing. We plan on irradiating the EGU at a later date in order to assess the performance of the FPA as a function of exposure to radiation.

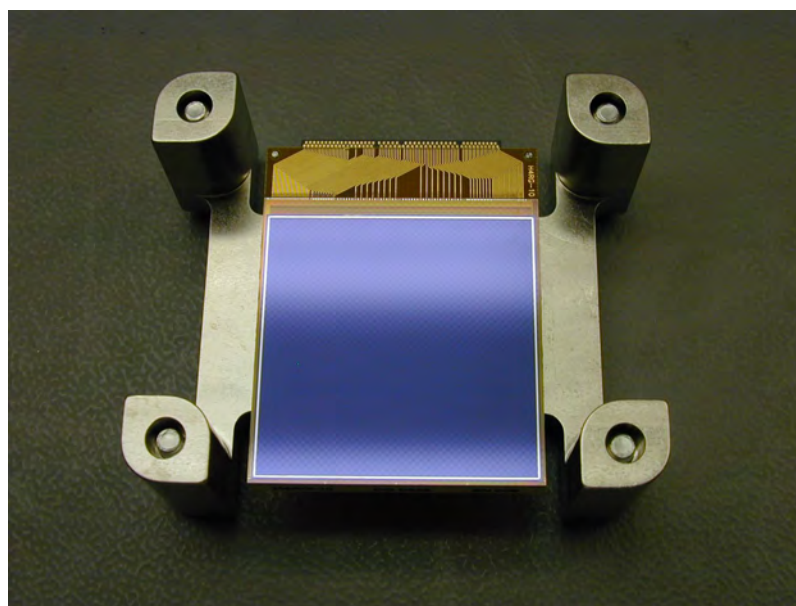


Figure 1. Science grade H4RG-10, delivered to USNO in Feb. 2007.

3. HIGH-SPEED, LOW-NOISE GROUND TEST CAMERA

In order to test and operate the FPA, USNO worked with GSFC/DSB/DCL (GSFC Code 553) to build a high-speed, low-noise ground test camera (GTC), shown in fig. 2 along with the two FPAs. The GTC was used both for laboratory testing and for observations at Flagstaff.

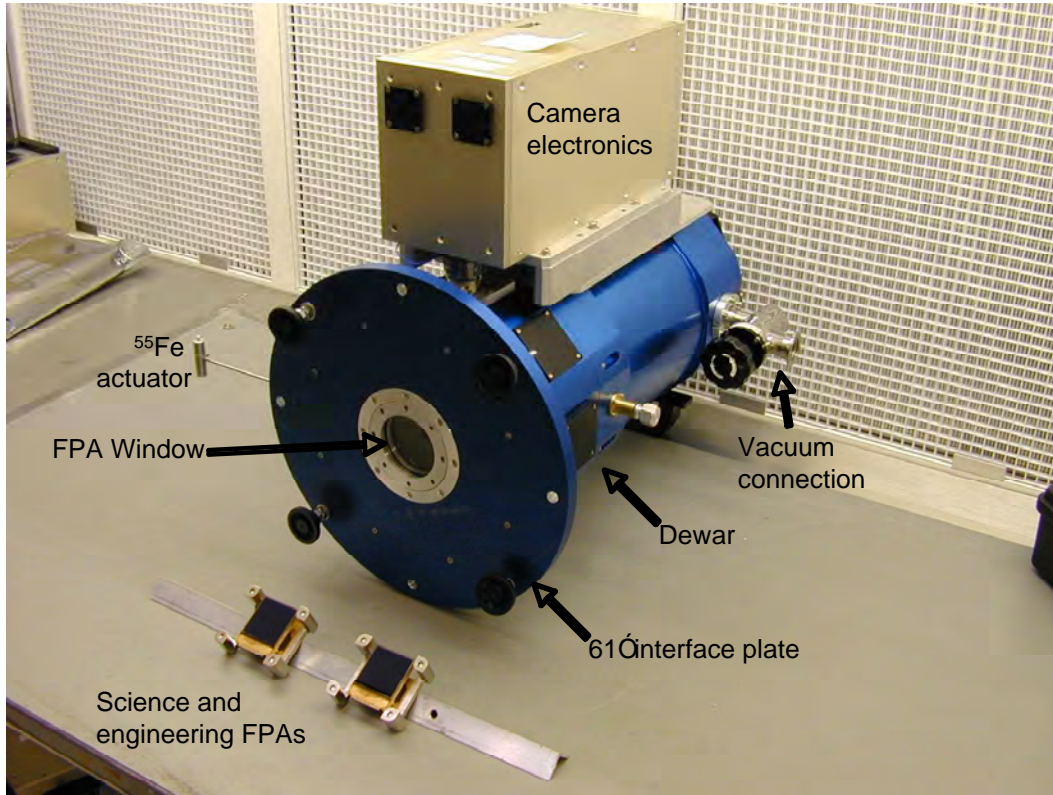


Figure 2. Ground test camera (GTC) shown with engineering and science FPAs.

The GTC consists of a 16-bit, 32-channel Leach camera electronics, a Universal Cryogenics dewar with 24-hour hold time, a Lakeshore temperature control unit, and a controller/data acquisition system. The GTC reads out the FPA using 32 (out of 64 available) ports operating at up to 400 kpix/channel/sec. As a result, the entire FPA can be read out in approximately one second. Because the system supports random access windowing, selected regions of the FPA can be read out at much higher frame rates without impacting performance.

The GTC was designed to be used with USNO's 61-inch Strand astrometric telescope located at NOFS. The design includes an ^{55}Fe source on a sliding actuator, allowing the FPA to be directly irradiated for purposes of gain calculation, cross-talk measurement etc. The camera can be operated at FPA temperatures* between 110 and 300 K, with a stability of 1 mK.

4. LABORATORY TESTING

The engineering and science grade units were tested in the GTC between March and May of 2007. Detector operating parameters were optimized to reduce read noise (see fig. 3). One of the first observations was that operating the detector at a bias voltage of 50 V vs. the suggested 16 V significantly improved performance across

* We note that the temperature sensor is not connected directly to the FPA but offset slightly. It is our assessment that the current set up results in, at most, a few-degree offset between the measured and actual temperatures. This offset has not been definitively determined. For purposes of this paper, we will refer to the measured temperature as the FPA temperature.

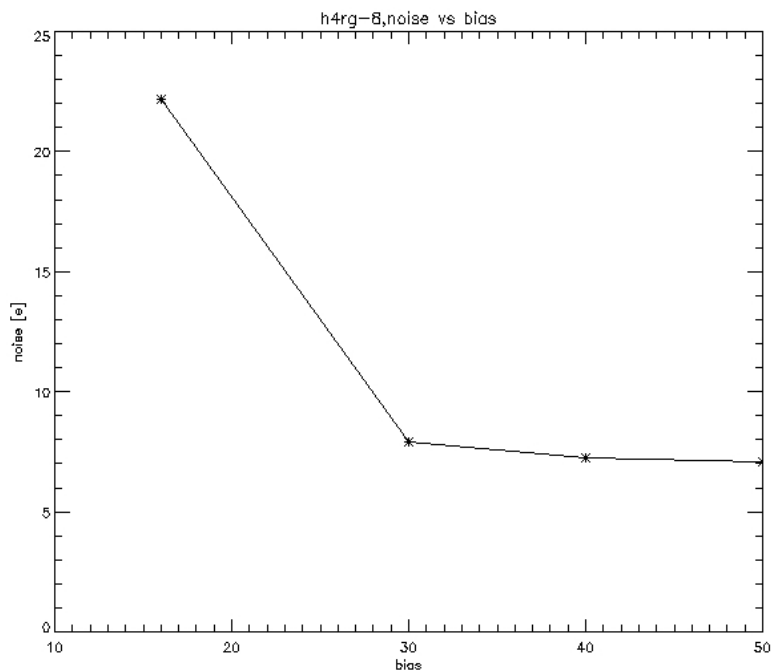


Figure 3. FPA read noise vs. bias voltage.

the board. There is some indication that raising the bias voltage above 50 V would lead to additional performance improvement, but given that TIS would only certify the FPA up to 50 V, higher bias voltage levels were not explored.

4.1 Read noise

Read noise was measured by resetting the FPA, reading out a reset noise reference frame, reading out an “image” frame, then differencing the reference frame from the image frame. A Gaussian function was then fit to the resultant distribution, with the width of the Gaussian defining the “post Correlated Double Sampling (CDS)” RMS read noise. The results (see fig. 3) indicate a read noise of 7 e- RMS at 50 V. Results were not corrected for the camera electronics noise although this noise component is negligible (< 2 e- RMS). This result is below the 10 e- read noise specification.

4.2 Spectral response

The quantum efficiency as a function of wavelength was measured using an integrating sphere and monochromator operating over 15 wavelengths spanning the range 400—1100 nm. Results are displayed in fig. 4.

As shown in the figure, between 625 and 850 nm, the QE peaks at above 90%. The detector meets the threshold and most of the objective QE requirements. The test FPA includes an AR coating that enhances near IR response; as such, the slight skew towards red response was not unexpected. It is believed that future FPAs with different AR coating would meet our requirements.

4.3 Pixel operability

As noted previously, one of our major concerns regarding CMOS-Hybrid focal plane technology is the ability to connect the detector pixels to the ROIC. The H4RG-10 has 16.7 million pixels, and each is relatively small when compared to earlier hybrids. As a result, the ability to align and connect the bonds within the appropriate tolerances so as to produce a large number of functioning pixels was assessed to be a major technical challenge with significant impact on overall detector yield. Since the program is ultimately interested in FPAs in the 8k x 8k class, any pixel operability problems experienced during the production of 4k x 4k devices would have significant implications for larger devices. As such, careful attention was paid to determining how many pixels were connected, and how well they were connected.

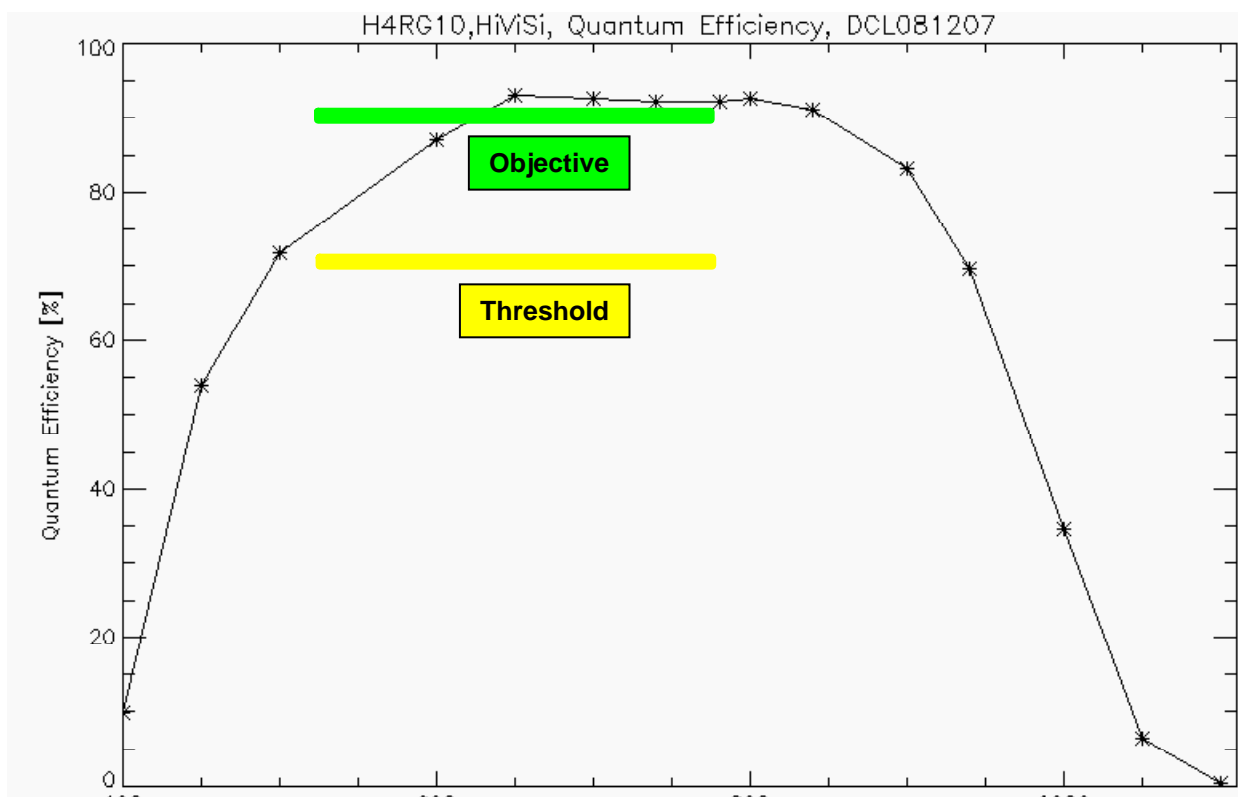


Figure 4. Measured quantum efficiency. Also shown are the threshold and objective requirements. The FPA had an enhanced red response due to the anti-reflective (AR) coating applied.

Pixel operability was measured by collecting flat field data. The FPA was exposed to a source of uniform illumination below saturation level and the resulting image was read out*.

The resultant distribution of pixel response is plotted in fig. 5. The figure shows the overall pixel response distribution (right panel) and the lower-end distribution (left panel). We note the bimodal distribution of the operability. The region near the primary peak contains most of the pixels. A secondary peak is present at very low connectivity level. A total of 4091 pixels were dead. Table 2 summarizes the cumulative results.

As shown in the table, adopting the flat-field response as the relevant metric for pixel connectivity and operability, essentially all pixels show connectivity, and nearly all (>99%) show high levels of response. The operability results are well above our requirements (see Table 1) of 96% (threshold)/99% (objective).

Table 2. Pixel flat-field response. The first column specifies the output signal threshold; the second column indicates how many pixels (and percentage) are “disconnected” at this level; the third column indicates percentage of connected pixels at the given threshold.

<i>Response level (relative to maximum response of 20,000 e-)</i>	<i>Pixels at or below threshold (%) (bad pixels)</i>	<i>% Pixels above threshold (good pixels)</i>
0 (not connected)	4091 (0.024%)	99.976%
10% (2000 e-)	8300 (0.05%)	99.95%
50% (10,000 e-)	33,400 (0.2%)	99.8%

* We note that the flat field was actually not flat, but had some signal variation due to test setup imperfections. This appears as a skew in the brightness level for the very brightest pixels in fig. 5.

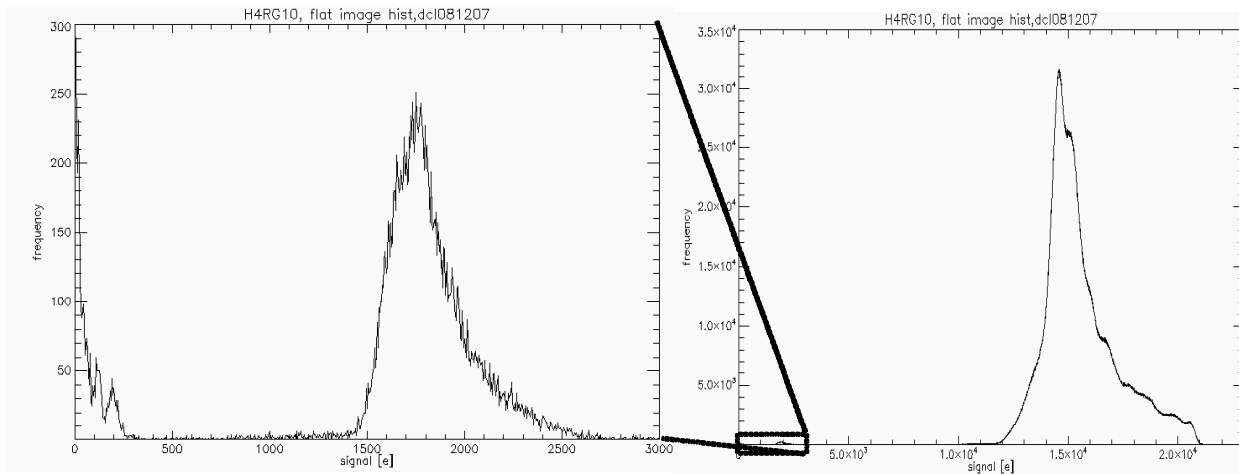


Figure 5. Pixel response distribution. (left) Distribution on lower end of response scale; (right) overall distribution. The position of the lower-end region within the overall distribution is indicated by the dotted box.

4.4 Cross-talk

Cross-talk was measured by irradiating the FPA with ^{55}Fe , locating the single-pixel events with symmetrical signal distribution in neighboring pixels, and comparing the signal in the central pixel with the signal in the surrounding pixels. The results are shown in fig. 6.

At the specified 16 V bias level, nearly half of the input signal is lost from the central pixel and winds up in adjacent pixels. Raising the bias level to 50 V increases the central pixel relative signal fraction to 0.7. From this we infer that the dominant source of cross-talk at 16 V is electron diffusion through the detector. At sufficiently high bias voltages, the FPA asymptotically approaches the inter-pixel capacitance limit. From the left panel in fig. 6, this appears to be at a central pixel fractional charge of about 0.7. At this limit, approximately 5% of the input signal is measured in each adjacent pixel.

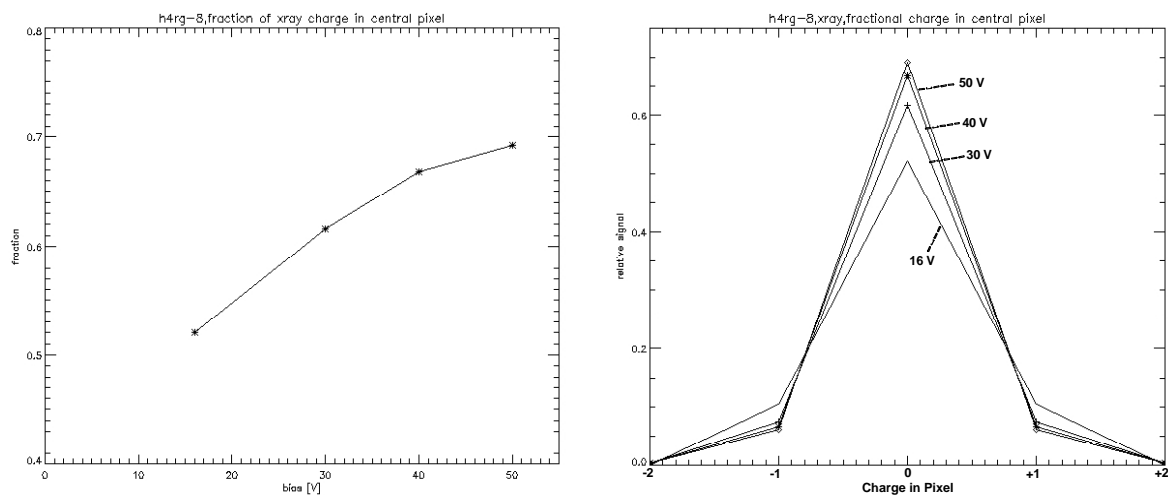


Figure 6. Cross-talk measurements. (Left) Signal in central pixel vs. bias voltage; (right) fractional signal distribution in central pixel vs. adjacent pixels (cross-section) for a range of bias voltages.

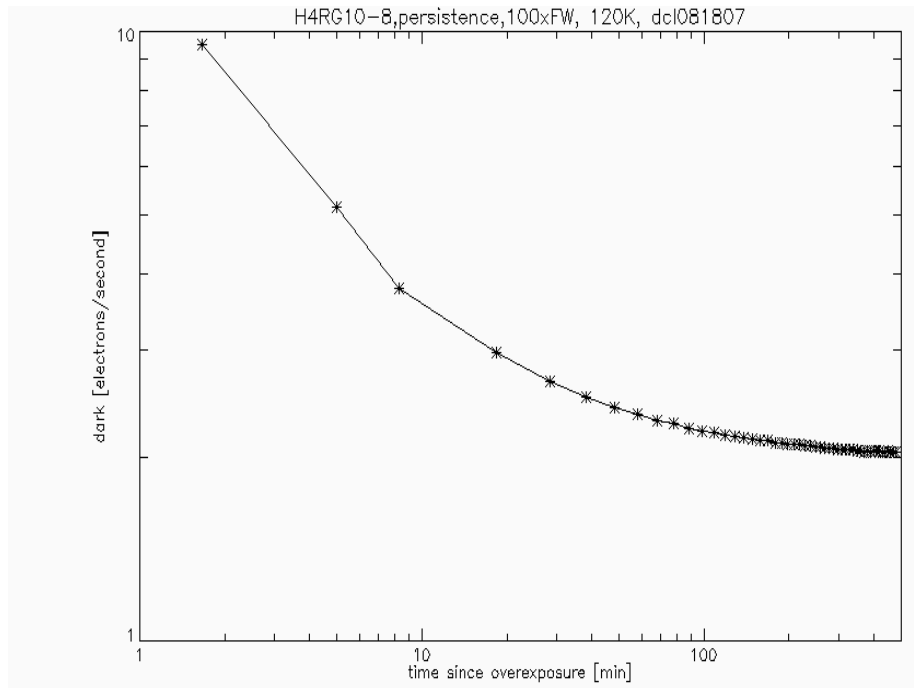


Figure 7. Persistence measurement after illumination with 100 x full well capacity. Electrons per pixel per second are shown, plotted as a function of time since illumination cut off.

4.5 Persistence

Persistence was measured by exposing the FPA to high levels of illumination then measuring signal levels at regular intervals after the illumination was removed. The results of one set of measurements are shown in fig. 7. The data were collected at 120 K after the FPA was illuminated with 100 x full well capacity. The figure shows the mode of the dark current distribution vs. time calculated in units of electrons per pixel per second.

FPA persistence is observed over the first two to three hours, but at relatively low rates. As shown in the figure, there is a dark current of approximately 2 e- per pixel per second. Persistence after two minutes is approximately 8 e- above dark, after ten minutes it is approximately 2 e- and after twenty minutes, it is 1 e- above dark. After two hours, it is approximately 0.1-0.2 e- above pre-illumination dark current. Persistence is believed to originate from traps in the detector material. In the case of the H4RG-10 we tested, these traps are the result of the fabrication process. One critical consideration for use in space is to measure the effect of exposure to radiation on persistence, since exposure to high energy proton flux that is typical of the space environment results in the generation of new traps in the detector material. This phenomenon will be measured at a later date.

4.6 Dark current

Dark level

Dark current measurements were made by covering the aperture and taking images using 90-second integration times. Reset frames were subtracted from the dark frames to remove most of the reset noise, and the images gain-corrected to electrons per second. The mode of the resultant distribution was taken to be the “dark current” level for a given temperature. Dark current measurements were collected over a range of temperatures from 110 K to 240 K. Measurements were made using both EGU and SGU and both before and after camera deployment to Flagstaff. The results are shown in fig. 8.

The FPA includes two types of “reference pixels.” Pixels of the first type are not connected to a photosensitive Si PiN diode, and terminate in a capacitor. The second are fully connected to the diode via the bump bonds, but are masked to light. Figure 8 also shows the results for the capacitively-terminated reference pixels (marked “Electronic Reference Pixels”).

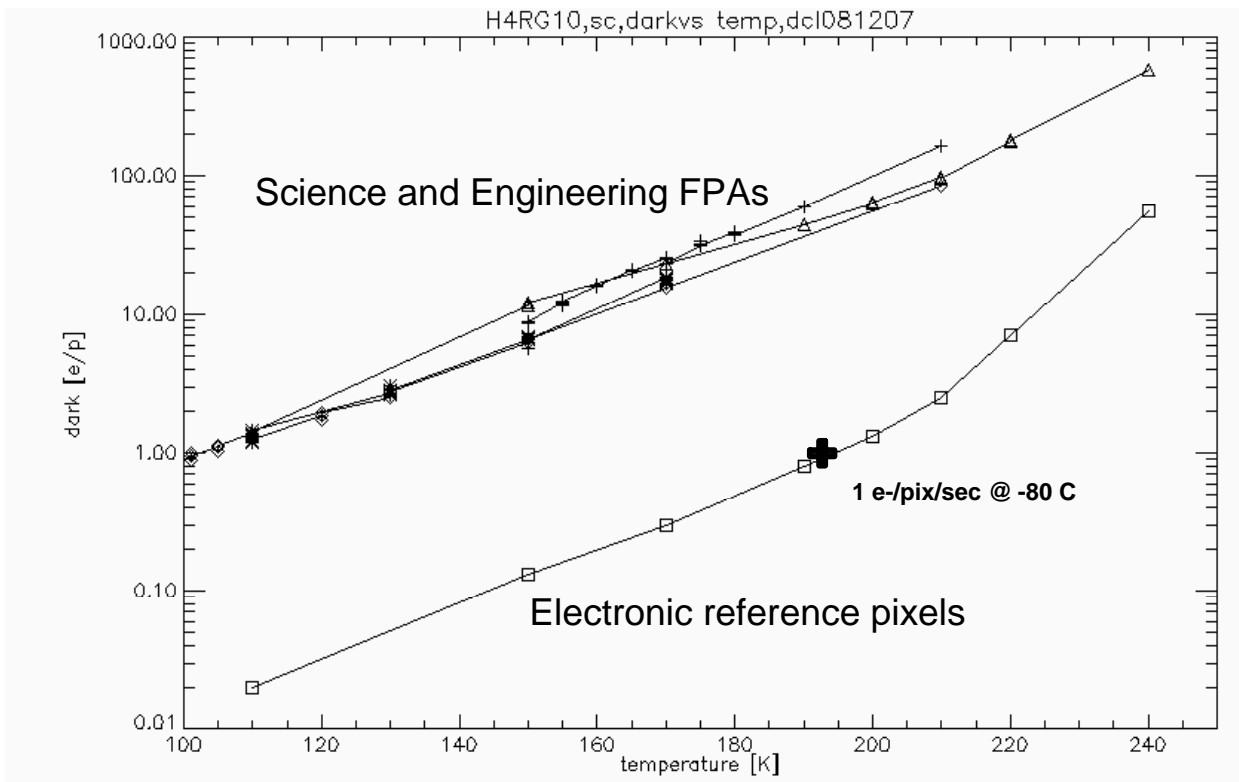


Figure 8. Dark current results for H4RG-10 science, engineering units and reference pixels. Also shown is the USNO requirement, indicated with a "+". Units are electrons per pixel per second. The “dark current” metric represents the distribution mode for a given temperature.

Also shown in the figure is the specification, viz., 1 e- per pixel per sec at a reference temperature of -80° C.

As is evident in the figures, the dark current is much higher (30—40x) than called for in the specification at the reference temperature. While the reference pixel level is high vs. reference pixel levels in other TIS devices (e.g., H1R measurements made by the authors for the WFC3 program), it is much lower than the dark current observed in the imaging pixels. This suggests some other mechanism is responsible for generating the very high dark levels observed in the imaging area.

Dark distribution

Beyond the single metric of mode (or median or mean, etc.), the distribution of the dark current is extremely important. In the left panel of fig. 9, the distributions for six different temperatures are shown. In the right panel, the cumulative distributions are shown. We note the relatively large number of hot pixels (i.e., dark current greater than the mode) when compared to similar plots of CCDs. These distributions are more like post-irradiation CCDs in terms of the relative number of hot pixels.

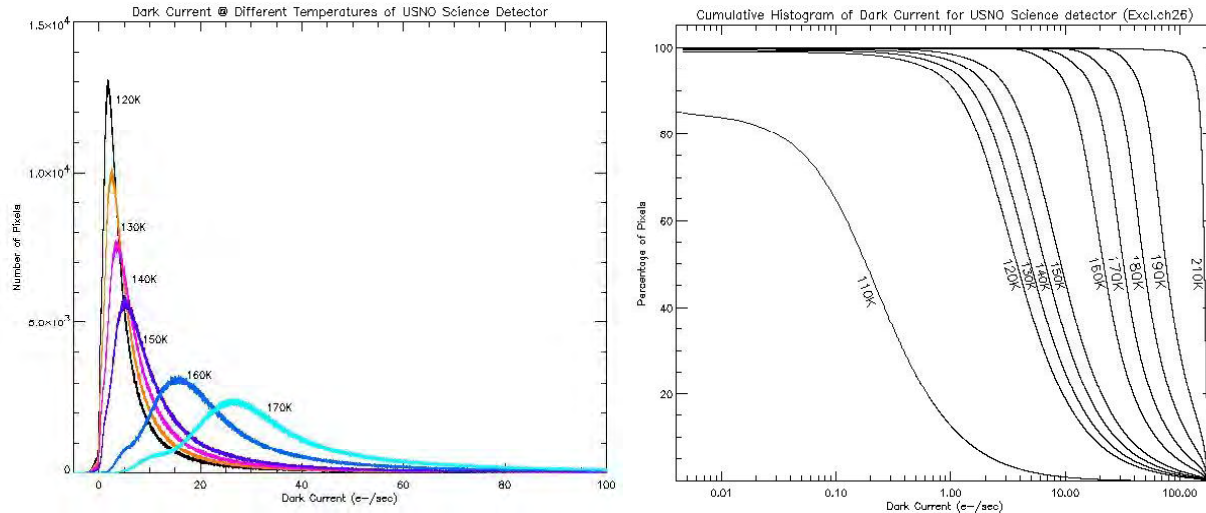


Figure 9. Distribution of dark current as a function of temperature. (Left) Distributions for six different temperatures; (right) cumulative distributions for ten temperatures. Note: this particular 110 K measurement is considered anomalous.

Dark spatial distribution

Within the dark current population, there appears to be some level of spatial correlation between the locations of “good” and “bad” (i.e., low and high dark current) pixels. Figure 10 shows two full-frame maps of the locations of the good pixels.

On the left, the positions of all pixels with dark currents of less than 0.5 e-/pix/sec are shown. On the right, the threshold is raised to 1 e-/pix/sec. First, we note the presence of the four rows of reference pixels around the

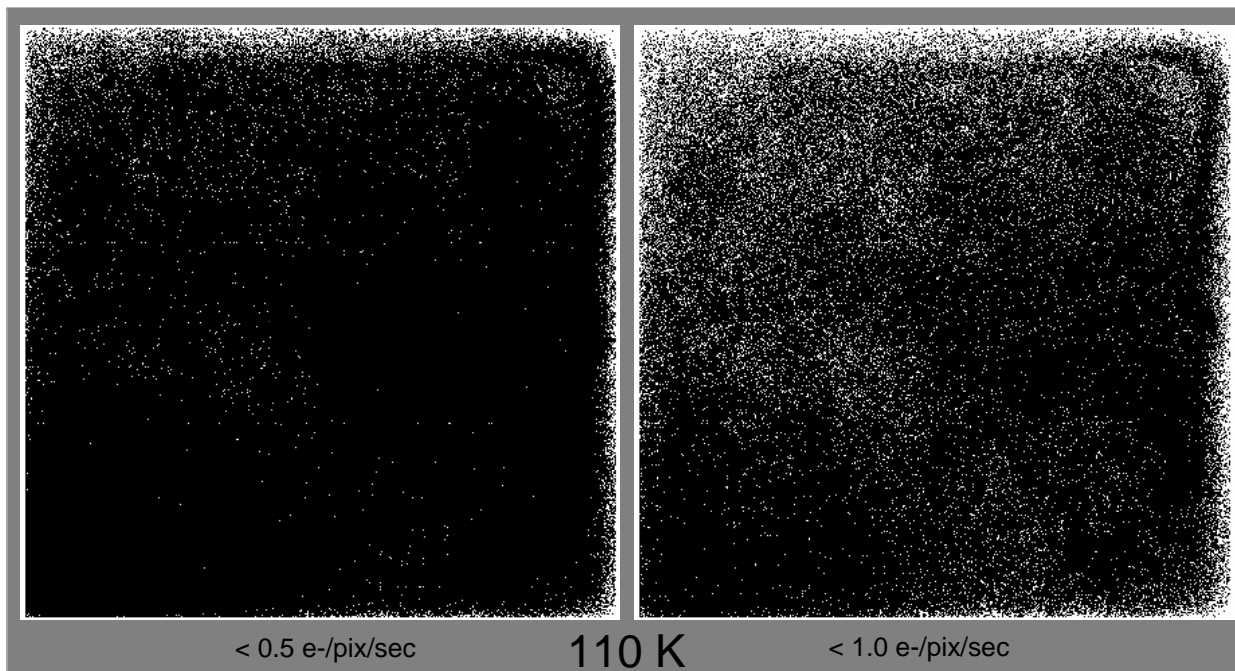


Figure 10. Low dark current maps. (Left) White pixels indicate location of pixels with < 0.5 e-/pix/sec dark current; (right) white pixels indicate location of pixels with < 1.0 e-/pix/sec dark current. Dark map taken at 110 K.

perimeter of the image. All electronic reference pixels meet the “good” pixel criterion. Next, we note that there is what appears to be a “picture frame” effect, wherein the good pixels seem to be preferentially distributed around the periphery of the array, especially along the right and upper edges. Finally, we note that there is additional spatial correlation, most evident in higher threshold image. These results are consistent with results from other H4RG-10 arrays, though these tend to show circular or spiral patterns [9].

Discussion

We will not speculate on the cause of the very high dark current in this paper except to observe that the spatial correlation of good vs. bad pixels may suggest a fabrication or hybridization process-related effect. The dark current and hot pixel population are high enough that even ground-based instruments running at 110 K are dominated by these effects. Pre-irradiation dark levels this high would pose a significant challenge for any space use, given the much higher costs associated with FPA cooling in space; furthermore, since a secular increase in dark and hot pixel population is a well-known phenomenon associated with exposure to the radiation present in space [10], the problem would significantly worsen over time. The high level of dark current and hot pixels is the most serious problem associated with the first-spin of H4RG-10 FPAs.

5. SKY TESTING AND ASTROMETRIC RESULTS

USNO’s primary interest in this detector is for potential future use in ground- or space-based astrometry programs. As such, the laboratory measurements described in §4 are important, but the final metric is the ability of the FPA to support high-precision astrometric and photometric measurements*. In order to test this, the camera was transported to NOFS and deployed onto the Strand 61-inch astrometric telescope. The Strand telescope is designed specifically for astrometry and is routinely used to take astrometric measurements at the few milliarcsecond level of precision.

5.1 Astrometric Methodology

The Strand telescope has a 1.55 m aperture, a focal length of 15.2 m and a resultant focal ratio of f/9.8. It has a plate scale of 13.5 arcseconds per mm, for a pixel scale of 135 mas per 10 μm H4RG-10 pixel; as a result, the 4k array subtends an area of approximately 9 arcminutes square on the sky when deployed on the Strand telescope.

The Ground Test Camera and science grade FPA were deployed to NOFS during early June, 2007. The globular cluster M13 was chosen as a convenient target, with multiple observations made of it over a variety of different filters, exposure times, gain settings, pointing orientations and FPA temperatures.

Observations and initial data processing

Science images were taken by first electronically resetting the FPA, then immediately reading out a CDS reference frame in a non-destructive fashion. The camera then non-destructively read out images at 30, 60, 120, 180 and 300 seconds. The CDS reference frame was subtracted from each image frame, resulting in a reset-corrected (i.e., CDS) image.

A reference set of dark images was collected during the observations. Because of different physical processes dominating in different pixels, the dark in some of the pixels were observed to scale linearly with time, while other pixels scaled exponentially. Attempts to generate a dark map that was a scalable over integration time did not prove to be fruitful. Instead, darks taken at the same exposure times and temperatures as the science images were used to create reference dark images. These reference darks were subtracted from the reset-corrected science images to create the final science image. Figure 11 is an example of one of the final science images. Figure 12 is a close-up of a region in fig. 11 and shows the pre- and post-dark-corrected images.

The effect of dark current on the images is apparent even at 110 K. Fortunately, the behavior of the pixels appears to be repeatable and stable over time periods of at least hour. The corrected image shows marked improvement over the uncorrected image. One artifact that does arise during the dark-correction process—especially for longer exposures and brighter stars—is the appearance of dark-induced saturation. Pixels that are saturated by dark current

* i.e., position and brightness measurements.

are set to zero during the correction process, even though they may have very high signals. This can be seen by the appearance of white (i.e., zero-signal) pixels in the PSFs of brighter stars in the corrected image in fig. 12

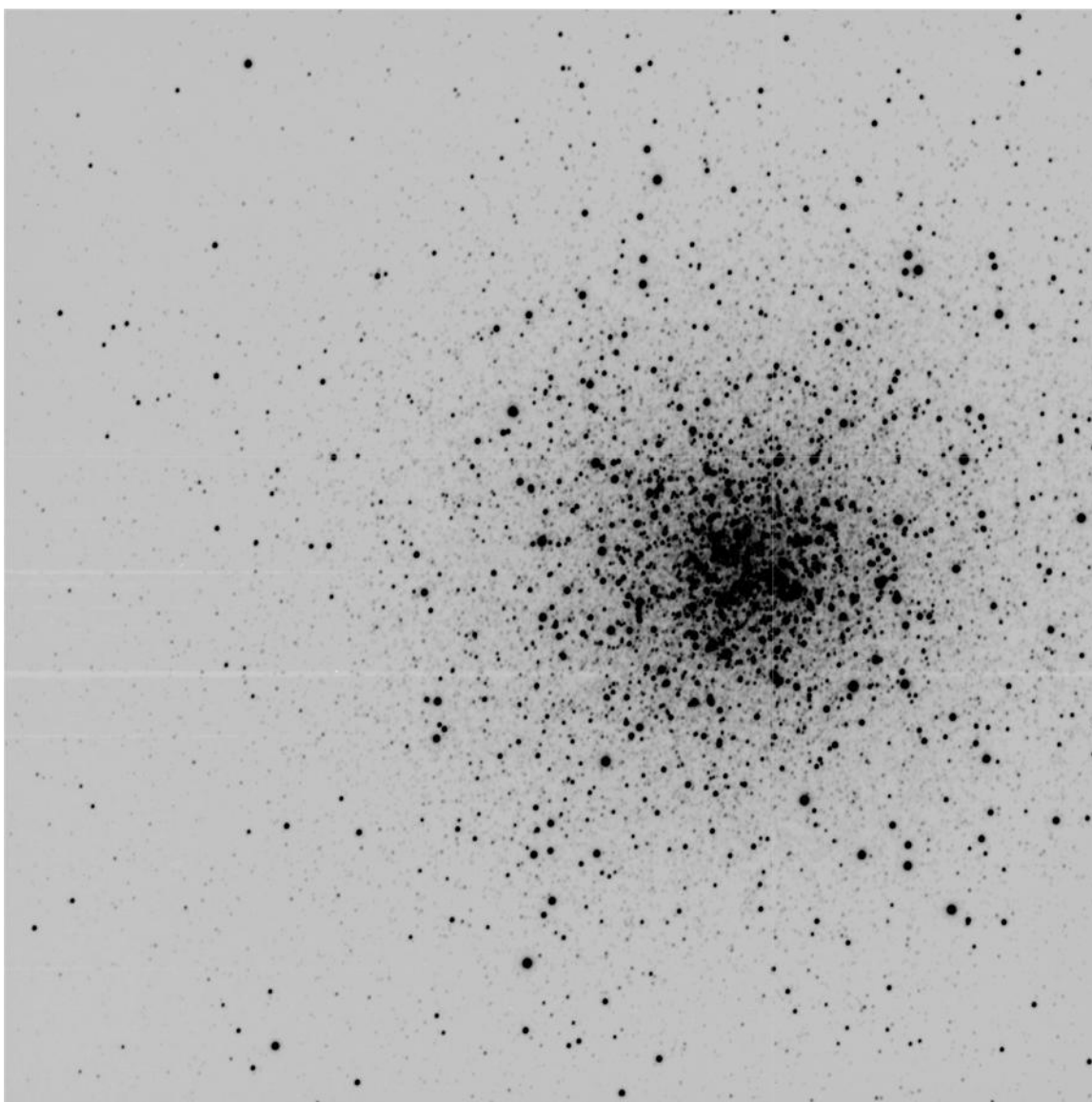


Figure 11. Processed full-frame H4RG-10 first light image of globular cluster M13. Exposure time is 360 seconds.

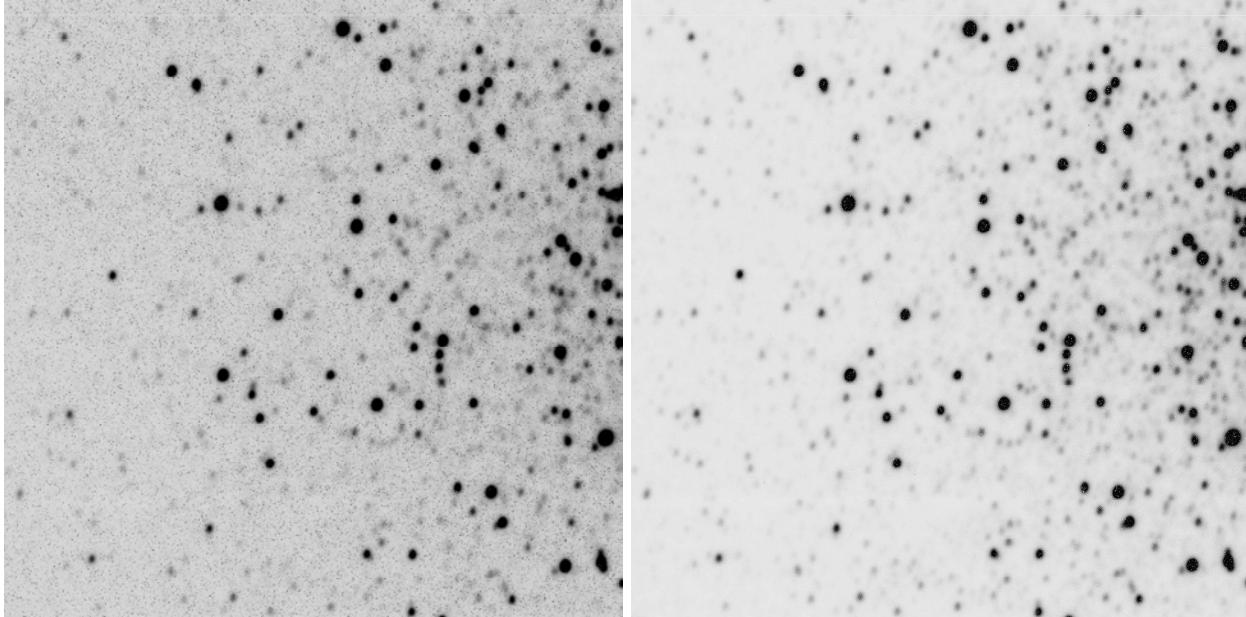


Figure 12 Close-up of M13 region showing effects of dark subtraction. (Left) Non-dark-subtracted image. (Right) Dark-subtracted image. Dark subtraction significantly improves the quality of the image by removing most of the effects of hot pixels, with the exception that bright stars are subject to "dark saturation" which appears as increased numbers of "zero signal" pixels within the bright star PSFs.

5.2 Astrometric Results

In order to determine the astrometric accuracy of the observations, a set of reference stars was identified in the data. Positions were extracted using the SExtractor routine [11] and a six parameter astrometric fit was performed using positions from the UCAC2 catalog [12]. All 60 exposures of this field were reduced this way and improved reference star positions calculated by minimizing the residuals. Comparing individual exposures with this improved reference catalog, an astrometric precision of 4 mas per coordinate for well-exposed stellar images on a single exposure was obtained, which is 1/30 of a pixel. Due to the high S/N, the centroiding precision (formal error from profile fitting) for these stars is negligible (of order of one milli-pixel). By using the methodology of Zacharias [13] and combining multiple exposure times, we predict that for arbitrarily long integration times (chosen to remove atmospheric noise rather than increase signal to noise ratio), the astrometric precision would approach 1/40th of a pixel (3 mas). Using a second method based on differential astrometry, we come up with 6 mas precision for the shorter exposures, scaling to 3 mas for longer exposures that suppress atmospheric effects. These results are consistent with other observations using the 61-inch, which also obtain about 3 mas per coordinate using a traditional CCD camera, and which indicate a camera-independent error floor. The 1/40th pixel precision is thus a worst-case estimate for the astrometric limit of the FPA.

5.3 "Qualitative" Multi-color photometric results

In order to get a qualitative sense of the photometric capabilities of the camera, multi-color data from the NOFS observations were used to generate a color-magnitude (C-M) plot of many of the observed sources. This analysis used data collected using two different filters on the 61-inch, but does not presently include precise calibration of the total in-band spectral response. Instead, a "rough calibration" was made using published stellar color data.

The results are shown in fig. 13. Data for a total of 1017 stars are displayed, with in-band photometry accurate to ~2%. Despite the rough color calibration, major astrophysical features are observed in the data, including the blue Horizontal Branch (BHB) stars, and the main sequence turn-off which is typically used to calculate the age of the

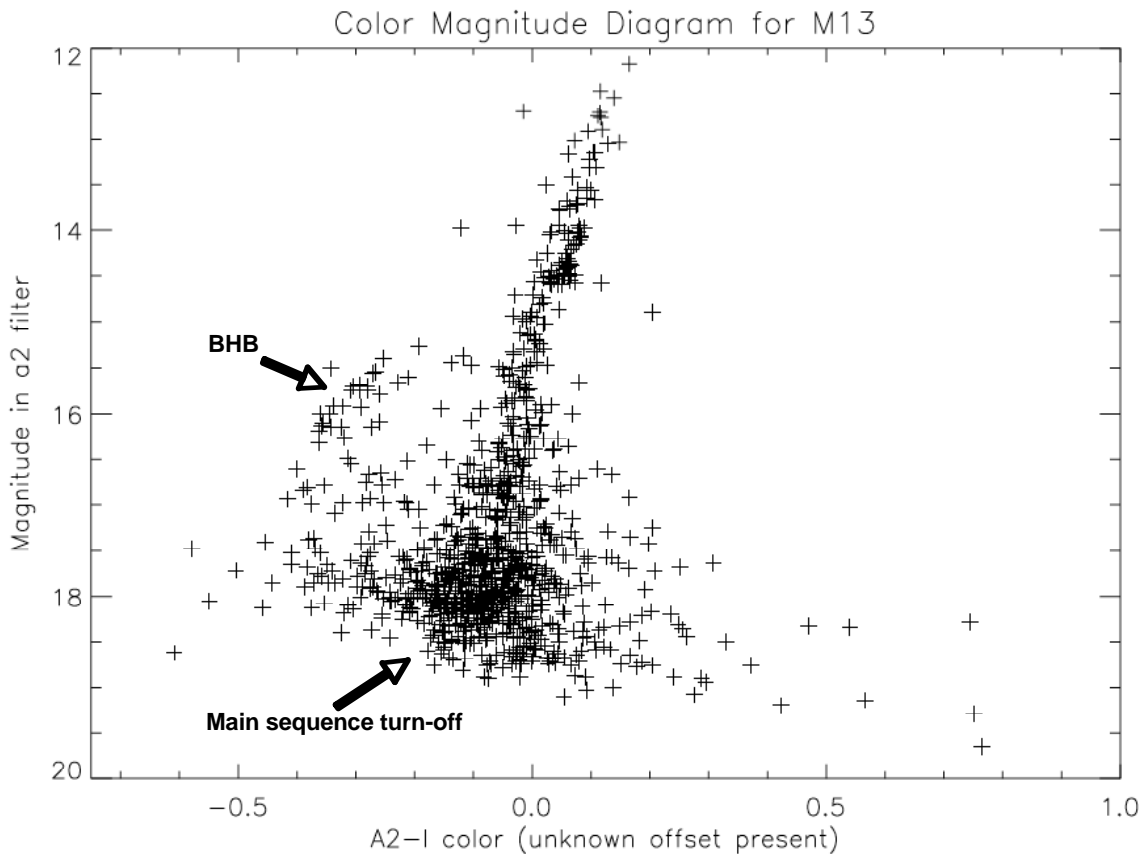


Figure 13. Color-magnitude diagram for M13. This represents a rough color calibration. Nevertheless, major astrophysical features are observed. “BHB” indicates location of blue horizontal branch stars.

cluster. The data compares favorably with that presented in Sandage [14] and Pyo & Lee [15]. From this, we conclude that the FPA is suitable for use in photometry. Further work will better quantify the multi-color photometric performance of the camera and FPA.

6. SUMMARY AND CONCLUSIONS

TIS has fabricated and delivered FPAs from the first spin of the H4RG-10 CMOS-Hybrid design. The science grade FPA tested by USNO at DCL and NOFS was found to have very high levels (>99%) of pixel connectivity and operability, lower than expected read noise (~7 e- RMS), and a spectral QE comparable to backside CCDs. Operating the FPA at higher voltages resulted in reduced pixel cross-talk, which was measured at about the 7% level. Persistence was found to be at the one e-/pix/sec level after a few tens of minutes, and at the tenths of an e-/pix/sec an hour after exposure of the array to 100 x full well capacity illumination. The FPA was found to support a variety of flexible readout capabilities, including: non-destructive read, random reset and random access windowing. The primary problem found with the FPA was that the dark current was measured to be 30—40 x higher than the specification, and that there was a disproportionately high population of hot pixels.

USNO deployed the H4RG-10-based ground test camera to its observatory in Flagstaff, AZ. The camera was used on the 61-inch Strand astrometric telescope to take images of the globular cluster of M13. The various observing modes of the camera, including non-destructive read, random pixel reset and CDS processing were demonstrated. The CDS and dark image subtraction processing routines were found to significantly improve the raw data, though numerous dark-related artifacts remain even after correction. An astrometric precision upper limit of 1/40th of a pixel was established for astrometric use of the FPA.

6.1 Conclusions

TIS has demonstrated the ability to produce H4RG-10 FPAs with high levels of pixel connectivity. The science grade unit that was tested met or exceeded requirements for many of the specifications. The most serious problem that arose during testing was the excessively high level of dark current. Both the overall level of dark current and the disproportionately large population of hot pixels need to be remedied before this FPA becomes competitive for use in space-based astrometric missions.

7. FUTURE WORK

USNO and GSFC plan to continue to develop the camera capabilities, and to redeploy the camera to the NOFS 1.3 m for additional field testing. This testing will attempt to push the astrometric precision below $1/40^{\text{th}}$ of a pixel. We will also use the opportunity to demonstrate more advanced windowing capabilities currently under development. In addition, USNO intends to perform radiation testing on the FPA to assess radiation hardness and suitability for use in space. These results will be reported on at future meetings.

Based primarily on the dark current results, another spin of FPAs that includes design or process modifications that address the dark current problems is indicated.

ACKNOWLEDGMENTS

The authors would like to acknowledge the excellent support provided for these observations by the staff at the Naval Observatory Flagstaff Station (NOFS), including Dr. Jeff Pier and Mike DiVittorio. We would also like to thank Dr. June Tveekam (GSFC) for issues related to design and fabrication of the camera window and Tom Hartman (GSFC) for his assistance during the deployment, operation and retrieval of the camera in Flagstaff, and to the GSFC DCL team that supported the fabrication and testing of the camera and FPAs.

REFERENCES

1. Dorland 2004, "Modeling the effects of proton damage to CCDs on astrometric measurement precision," Proc. SPIE, 5167, 302
2. Dorland, B. N. et al. 2007, "Astrometric sky testing results for the TIS 5-micron 3T-class CMOS detector," Proc. SPIE 6690-19
3. Kessel, R.A., et al. 2007, "Radiometric and Noise Characteristics of SI-1920HD Cameras Built from the AltaSens ProCamHD 3560 FPA", Proc. SPIE, 6690, 18
4. Janesick, J.R. 2004, "Charge Coupled CMOS and Hybrid Arrays," Proc. SPIE, 5167, 1
5. Beletic, J. 2006, private communication
6. Pool, P. 2006, private communication
7. Bai, Y. et al. 2005, "Recent Progress of Hybrid CMOS visible focal plane array technologies," Proc. SPIE, 5902-27
8. Beletic, J. 2006, private communication
9. Beletic, J., 2007, private communication
10. Polidan, E. et al. 2004, "Hot pixel behavior in WFC3 CCD detectors irradiated under operational conditions," SPIE Proc. 5167, 258
11. Bertin, E., & Arnouts, S. 1996, "SExtractor: Software for source extraction," A&A Sup., 117, 393
12. Zacharias N., et al. 2003, "The USNO CCD Astrograph Catalog (UCAC) Project and Beyond," Astrophysics and Space Science Library, 288, 67
13. Zacharias, N. 1996, "Measuring the Atmospheric Influence on Differential Astrometry: A Simple Method Applied to Wide Field CCD Frames," Publications of the Astronomical Society of the Pacific, 108, 1135
14. Sandage, A. 1970, "Main-sequence photometry, color-magnitude diagrams, and ages for the globular clusters M3, M13, M15, and M92," Astrophysical Journal, 162, 841
15. Pyo, T.S. & Lee, S.-W. 1994, "The BVR CCD Photometry of Globular Cluster M13," Journal of Korean Astronomical Society, 27, 119